Dentomaxillofacial Radiology (2013) 42, 20130035
© 2013 The Authors
http://dmfr.birjournals.org

TECHNICAL REPORT

Multiobjective optimization framework for landmark measurement error correction in three-dimensional cephalometric tomography

A DeCesare[1], M Secanell[1], MO Lagravère*[,2] and J Carey[1]

[1]Department of Mechanical Engineering, Faculty of Engineering, University of Alberta, Edmonton, AB, Canada; [2]Department of Dentistry, Orthodontic Graduate Program, Faculty of Medicine and Dentistry, University of Alberta, Edmonton, AB, Canada

The purpose of this study is to minimize errors that occur when using a four *vs* six landmark superimpositioning method in the cranial base to define the co-ordinate system. Cone beam CT volumetric data from ten patients were used for this study. Co-ordinate system transformations were performed. A co-ordinate system was constructed using two planes defined by four anatomical landmarks located by an orthodontist. A second co-ordinate system was constructed using four anatomical landmarks that are corrected using a numerical optimization algorithm for any landmark location operator error using information from six landmarks. The optimization algorithm minimizes the relative distance and angle between the known fixed points in the two images to find the correction. Measurement errors and co-ordinates in all axes were obtained for each co-ordinate system. Significant improvement is observed after using the landmark correction algorithm to position the final co-ordinate system. The errors found in a previous study are significantly reduced. Errors found were between 1 mm and 2 mm. When analysing real patient data, it was found that the 6-point correction algorithm reduced errors between images and increased intrapoint reliability. A novel method of optimizing the overlay of three-dimensional images using a 6-point correction algorithm was introduced and examined. This method demonstrated greater reliability and reproducibility than the previous 4-point correction algorithm.
Dentomaxillofacial Radiology (2013) **42,** 20130035. doi: 10.1259/dmfr.20130035

Cite this article as: DeCesare A, Secanell M, Lagravère MO, Carey J. Multiobjective optimization framework for landmark measurement error correction in three-dimensional cephalometric tomography. *Dentomaxillofac Radiol* 2013; **42:** 20130035.

Keywords: cone beam computed tomography; orthodontics; maxillary expansion treatment; landmark optimization procedure

Introduction

The use of three-dimensional (3D) imaging for orthodontic diagnosis and treatment planning is increasing.[1] Cone beam CT (CBCT) is one technology easing the transition and increasing the accessibility for dental professionals.[1,2] The CBCT technology provides geometrically accurate 3D visualization of anatomical structures while overcoming the distortion of traditional two-dimensional (2D) imaging. It also allows axial, coronal and sagittal dimensional evaluations through slices.[2,3] The use of CBCT can help professionals to better understand the results of their treatments and allow for better diagnosis and patient treatment plans. Nevertheless, the use of CBCT needs to follow careful cost *vs* benefit analysis and needs to practice "as low as reasonably achievable" principle on a case-by-case basis. Another potential advantage of CBCT 3D imaging currently being evaluated is the possibility of analysing skeletal changes resulting from growth or treatment by using image superimposition. Superimposition has been done traditionally using lateral cephalograms providing 2D skeletal changes.[4] However, methods currently used

---

*Correspondence to: Dr Manuel O Lagravère, Room 5-524, Edmonton Clinic Health Academy, University of Alberta, Edmonton, AB, Canada T6G 1C9. E-mail: manuel@ualberta.ca

Received 25 January 2013; revised 5 April 2013; accepted 11 April 2013

for image superimposition using 3D CBCT images still need improvement.[5–7] The alignment problem between two images taken at different times can be seen in Figure 1.

To superimpose 3D images, a stable skeletal structure must be selected to define a reference co-ordinate system. Several studies[6,8–10] have proposed the use of the cranial base, since this is considered to be a stable area by the time the orthodontic-patient treatment begins. Most of the cranial base growth (more than 85%) occurs in the first 5 years after birth, with only minor changes afterwards.[11,12] Accuracy and reliability studies of landmark locations in CBCT images have been published.[13–16] Few articles, however, have reported the use of cranial base landmarks to determine the reference co-ordinate system for pre- and post-treatment image superimposition.[4,17–20] It has been reported that using cranial base landmarks to define the reference co-ordinate system is not simple and needs improvement, since minor errors in landmark location can magnify the errors of landmarks of interest located far away from the origin of the co-ordinate system.[7,17] One issue is that software cannot identify the centre of landmarks, requiring methods to realign the images. Recently, Lagravère et al[21] proposed a methodology to correct for measurement errors using four points.

The purpose of this study is to minimize errors that occur during image superimposition. This will be done by first evaluating the use of four *vs* six landmarks in the cranial base to define the co-ordinate system followed by evaluating if the use of more landmarks reduces the errors associated with the superimposition of serial CBCT images utilizing the co-ordinate system created using four *vs* six landmarks.

Materials and methods

The investigators recognize the controversial risk of CBCT scanning on children. The current study is a retrospective study of gathered data. CBCT volumetric data were taken using a NewTom 3G Volumetric Scanner (NewTom, Aperio, Italy) at 110 kV, 6.19 mAs and 8 mm aluminium filtration. Data from ten patients participating in a maxillary expansion clinical trial were used for this study. Ethics approval was received by the institutional health ethics board (study number 5563). Images were taken using a 12-inch detector field at baseline before any treatment was done to the patients.

Images were obtained and converted to Digital Imaging and Communications in Medicine (DICOM) format using the NewTom software (Aperio, Italy) with a voxel size of 0.25 mm. Using AVIZO software (AVIZO, Visualisation Sciences Group, Burlington, MA), the DICOM format images were rendered into a volumetric image using 512×512 matrices giving a range of 400–420 DICOM slices. Sagittal, axial and coronal volumetric slices, as well as the 3D image reconstructions, were used to determine the landmark positions. Procedures and definitions for landmark location in this study followed that of previous studies.[7,8,15–17]

Four landmarks are required to define a 3D anatomical reference co-ordinate system. The left and right auditory external meatus (AEML and AEMR, respectively) and the dorsum foramen magnum (DFM) were selected based on the position and early formation in skeletal growth. The fourth point, ELSA, is defined as the midpoint between the left and right foramen spinosum.[22] ELSA was selected as the origin of the new Cartesian co-ordinate system. From the origin, 3D positional co-ordinates for the AEML, AEMR and DFM were determined. Intrareliability values were determined using intraclass correlation coefficient for all four landmarks, repeating the process three times for each image. Intrareliability values for each Cartesian co-ordinate for all landmarks were reported being the lowest, with a value of 0.965, in the x-axis for the AEML.[7]

Landmarks used in the present study are ELSA, AEML, AEMR, DFM, right foramen ovale (RFO) and left foramen ovale (LFO) as well as infraorbitals (right

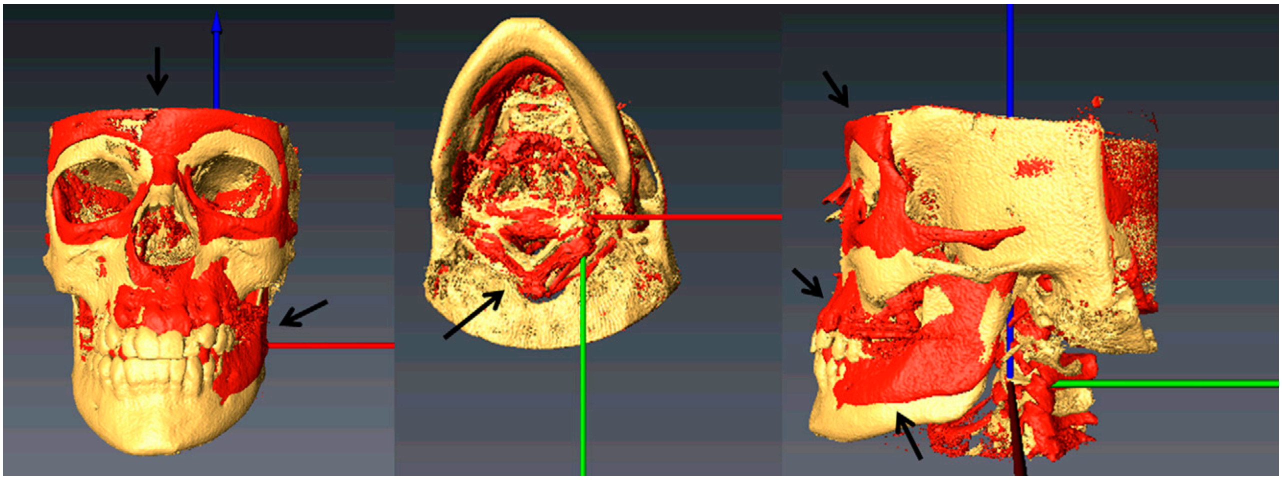

Figure 1 Misalignment present between two images of the same patient taken at different time points during treatment. Arrows indicate the different areas of misalignment between the two images in the three views

and left) and mentons (right and left). The principal investigator, an orthodontic specialist with PhD research experience in landmark location in CBCTs, located the landmarks on each image three times. In AVIZO, spherical markers of 0.5 mm diameter were placed indicating the position of the landmark, and the software used the centre of these spherical markers as the coordinates.

First co-ordinate transformation procedure

A detailed description of the transformation process is given in the study by Lagravère et al.[21] Using an initial co-ordinate transformation, values were obtained for the new infraorbitals (right and left) and mentons (right and left) landmarks. Images were measured three times, and thus it was expected that an error close to zero would be obtained based on previous results. After the analysis was done, a second transformation was performed on the four initial points.

Novel second co-ordinate transformation procedure involving six landmarks

The relative position of the AEML, AEMR and DFM landmarks with respect to ELSA should be the same between two images. Additionally, the position of AEML, AEMR and DFM with respect to each of the additional two points, *i.e.* RFO and LFO, should also remain the same between both images. However, owing to operator errors, small differences in the co-ordinates are observed between the images. To correct the measurement errors, an algorithm was developed to determine the corrections necessary in the location of AEML, AEMR and DFM, since these define the co-ordinate system in the image. This was done to ensure that the distances and angles between AEML, AEMR, DFM and ELSA and the distances and angles between AEML, AEMR, DFM and the two additional static points (RFO and LFO), which provide additional metrics to measure the operator error, are maintained. To achieve this, an error correction vector for each point that was used to define the co-ordinate system in Image 2 (*i.e.* $\delta\mathbf{u}_{\mathrm{AEML}}$ for AEML, $\delta\mathbf{u}_{\mathrm{AEMR}}$ for AEMR and $\delta\mathbf{u}_{\mathrm{DFM}}$ for DFM) was obtained. Vectors $\delta\mathbf{u}_{\mathrm{AEML}}$, $\delta\mathbf{u}_{\mathrm{AEMR}}$ and $\delta\mathbf{u}_{\mathrm{DFM}}$ define the co-ordinate system corrections such that the points AEML, AEMR, DFM and ELSA in Images 1 and 2 have a minimum difference in relative distances and angles between each other as well as to RFO and LFO.

To obtain the error correction for AEML, AEMR and DFM in Image 2, a multiobjective optimization problem needs to be solved. The goal is to minimize several objectives: (a) the difference between Image 1 and Image 2 in relative distance between AEML, AEMR and DFM as well as to RFO and LFO, and (b) the difference between Image 1 and Image 2 in relative angles between AEML, AEMR and DFM as well as to RFO and LFO. The list of objectives to be minimized is computed using several equations based on linear algebra and are given and explained in detail in the Appendix.

To combine the multiple objectives above into a single objective function, the weighted sum method is used.[23] The resulting multiobjective optimization problem is:

$$\text{Minimize} : \frac{1}{9}\sum_{i=1}^{9} w_{f,i} f_i + \frac{1}{12}\sum_{j=1}^{12} w_{g,j} g_j \tag{1}$$

$$\text{with respect to } \delta\mathbf{u}_{\mathrm{AEML}},\ \delta\mathbf{u}_{\mathrm{AEMR}} \text{ and } \delta\mathbf{u}_{\mathrm{DFM}} \tag{2}$$

$$\text{such that} : (-5,\ -5,\ -5) < \delta\mathbf{u}_{\mathrm{AEML}} < (5,\ 5,\ 5) \tag{3}$$

$$(-5,\ -5,\ -5) < \delta\mathbf{u}_{\mathrm{AEMR}} < (5,\ 5,\ 5) \tag{4}$$

$$(-5,\ -5,\ -5) < \delta\mathbf{u}_{\mathrm{DFM}} < (5,\ 5,\ 5) \tag{5}$$

where f_i is the primary objective to be minimized in the multiobjective optimization problem in Equation (1) and g_i is the secondary objective to be minimized in the multiobjective optimization problem in Equation (1), $\delta\mathbf{u}_{\mathrm{AEML}}$, $\delta\mathbf{u}_{\mathrm{AEMR}}$ and $\delta\mathbf{u}_{\mathrm{DFM}}$ are the correction factors for the AEML, AEMR and DFM points used to set up the reference frame in Image 2 and $w_{f,i}$ is the weight factor applied to the primary equations in the objective function in the multiobjective optimization problem in Equation (1) and $w_{g,j}$ is the weight factor applied to the secondary equations in the objective function in the multiobjective optimization problem in Equation (1). The weights are assigned according to the importance of the objective and must satisfy Equation (6):

$$\frac{1}{9}\sum_{i=1}^{9} w_{f,i} + \frac{1}{12}\sum_{j=1}^{12} w_{g,j} = 1 \tag{6}$$

In this article, the weight factors were selected as follows. Objective function equations were put into two groups. The first group, named primary objectives and represented by variables f_i, contained all the objectives that involved AEML, AEMR and DFM. These objective functions existed in the previous 4-point algorithm developed by the authors.[21] These constraint equations were treated as the most important, as they ensured that distances and angles between ELSA, AEML, AEMR and DFM were the same between the two images. All the equations in the first group were given equal weight factor, $w_{f,i}$. The sum of all weight factors was 0.9, *i.e.* $w_{f,j} = 0.1$. The rest of the constraint equations, named secondary equations, and represented as g_i, are those objectives related to points LFO and RFO. These objectives are critical for determining a unique solution. These secondary constraints were treated as less vital since they are used mainly to refine the search and, therefore, were given a smaller weight factor. All weight factors $w_{g,j}$ were given equal importance, and their sum was set to 0.1 so that Equation (6) was satisfied. Therefore, the value of each factor is $w_{g,j} = 0.0083$. It should be noted that different values for $w_{f,i}$ and $w_{g,j}$ could be used instead of the proposed 0.9 and 0.1, such as 0.8 and 0.2; however, based on a parametric study for weight values in the range of 1–0.8 and 0–0.2 for $w_{f,i}$ and $w_{g,j}$, respectively, the proposed weights were shown to provide more accurate results for several of the validation studies under consideration. Given a new system of landmarks, a similar parametric study should be performed for selecting the weights.

The correction factors, $\delta\mathbf{u}_{\mathrm{AEML}}$, $\delta\mathbf{u}_{\mathrm{AEMR}}$ and $\delta\mathbf{u}_{\mathrm{DFM}}$, were bound because it was known that the optimized positions of each point must lie relatively close to the originally identified point locations. Although mathematically there may exist solutions outside these bounds, these solutions are not feasible and must be excluded *a priori* from consideration.

The optimization problem has nine design variables corresponding to the measurement error correction in each direction for AEML, DFM and AEMR. These design variables are crucial because they each modify a point used in the co-ordinate system transformation; therefore, any changes made to them will indirectly modify the location of all other points identified.

The optimization problem aims at minimizing the difference in distance and angle between the points. The final optimization problem is difficult to solve. It contains several local minima, of which only the global minimum is desired. Therefore, a genetic algorithm was chosen owing to its resiliency to local minima and the ability to find a global solution. The genetic algorithm used is the MATLAB (Mathworks Inc., Natick, MA) genetic algorithm routine, named "ga()". To solve the problem, an initial population size of 10 000 was used. The algorithm-specific input parameters used in this research are given in Table 1.

Our algorithm guarantees that the distance between ELSA and AEML and AEMR and DFM are as close as possible for the two images and that the relative distances between AEML and AEMR, AEML and DFM, AEML and RFO, AEML and LFO, AEMR and DFM, AEMR and RFO, AEMR and LFO, DFM and RFO and DFM and LFO are as close as possible between Images 1 and 2, respectively; and, finally, that all angles are as close as possible.

Validation studies

A test was devised to test the repeatability of the 4-point algorithm (AEML, AEMR, ELSA and DFM) *vs* the 6-point algorithm (AEML, AEMR, ELSA, DFM, RFO and LFO). Owing to the voxel size of 0.25 mm, it is unknown where the landmark truly lies within the sphere of error. To examine the potential effect this uncertainty could have on the final result, the points on the second image were displaced in a random amount ranging between 0 mm and 0.25 mm within the maximum landmark detection error in each direction. Then, each set of perturbed points with randomized errors were corrected relative to the first image with both the 4-point and the 6-point algorithms. The suggested solutions for each code were recorded. To verify the reliability of this new algorithm, five test cases were conducted by identifying the location of several static points on two different images using both the 4-point and 6-point correction algorithms. To further validate the reliability of this method, 100 cases with a random measurement error were analysed using the 6-point correction.

Table 1 Genetic algorithm-specific parameters

Genetic algorithm options	
Mutation function	Mutation gaussian
Cross-over function	Cross-over scattered
Selection function	Selection tournament
Hybrid function	@fmincon
Generations	1000
Population size	10 000
Convergence tolerance	1.00×10^{-05}

Clinical studies

Real data for ten patients were analysed using both the 4-point and 6-point correction algorithms. Each of the ten patients had two images taken 12 months apart, and in each case, the second image was corrected relative to the first image. To ensure repeatability, each patient's data set was corrected ten times with each algorithm, and the average correction factors were found. Four points, infraorbitale left, infraorbitale right, menton left and menton right, were used as the controls points to quantify the success of each correction method. Each of these control points are expected to remain unmoved between images, and thus their distances relative to the three points used to construct the co-ordinate system (AEML, AEMR and DFM) should remain constant between the first and second images for each patient. The images used were from patients in a group age where transverse growth has had its most significant changes, thus further transverse growth-based changes were neglected. No studies were found that assessed the 3D position changes in these specific landmarks within this age group; thus it was considered that these landmarks may have minor, but not significant, position changes as a result of growth within our 1-year imaging time frame.

The average error for each control point is obtained by first finding the distance between that control point and each of AEML, AEMR and DFM in the first image for each patient. Those same distances are then found in the second image. The error reported is the absolute value of the difference in distances between points calculated for the first image and the second image. These calculations are repeated after the positions of AEML, AEMR and DFM have been optimized with the 4-point algorithm and then repeated again after the positions of AEML, AEMR and DFM have been optimized with the 6-point algorithm. The overall average error is found by averaging the errors between all the points for all the patients.

Results

Validation studies

Five test cases were analysed using both the 4-point and 6-point correction algorithms, and results for this study are given in Table 2. The 4-point algorithm proposed in Reference 20 converged to a new, distinct solution every time. The 6-point algorithm with a genetic algorithm optimizer converged to a nearly identical solution in Trials 1, 3, 4 and 5 (seen in bold) and a separate solution in Trial 2 (seen in italics). The advantages of the new 6-point algorithm include much higher intertest reliability and greater consistency between trials.

It should be noted, as seen in the tables, that the previous method sometimes provided a better solution; however, it was suggesting a different optimal position in every trial. An unstable set of solutions is not desired. Results show that the new method is able to converge to the same solution from different starting points across multiple trials.

The final validation of the reliability of the 6-point correction method was done using 100 cases with a random measurement error. Figure 2 shows that 52% of these solutions converge to the first major global solution and a further 44% of these solutions converge to a second major global solution, meaning that a total of 96% of results converged to one of two specific solutions.

Clinical studies

The results of the clinical study can be seen in Table 3 and are summarised in Table 4. As can be seen in Table 3, the 6-point algorithm provided the best solution with the lowest average distance error for every single control point. It should be noted that in some cases, the distance errors actually increased after optimization, most notably seen in Table 3(d) where the

Table 2 Experimental results of five trials with randomized errors

		Perturbed points			*Suggested solution*		
Trial 1, genetic	ELSA	0.00	0.00	0.00	**0.00**	**0.00**	**0.00**
	AEML	58.00	17.10	−0.19	**58.13**	**15.50**	**−3.18**
	AEMR	−57.46	14.89	−0.20	**−57.34**	**16.09**	**0.00**
	DFM	−0.11	49.63	−28.69	**0.19**	**46.46**	**−33.74**
Trial 2, genetic	ELSA	0.00	0.00	0.00	*0.00*	*0.00*	*0.00*
	AEML	58.07	16.73	0.24	*57.87*	*16.71*	*0.36*
	AEMR	−57.44	14.82	0.15	*−57.66*	*14.86*	*0.01*
	DFM	−0.18	49.57	−28.71	*0.16*	*50.21*	*−27.87*
Trial 3, genetic	ELSA	0.00	0.00	0.00	**0.00**	**0.00**	**0.00**
	AEML	57.98	17.13	0.08	**58.13**	**15.54**	**−3.10**
	AEMR	−57.90	15.00	0.22	**−57.35**	**16.04**	**0.00**
	DFM	0.09	49.73	−28.79	**0.18**	**46.56**	**−33.60**
Trial 4, genetic	ELSA	0.00	0.00	0.00	**0.00**	**0.00**	**0.00**
	AEML	57.78	16.98	−0.16	**58.13**	**15.55**	**−3.06**
	AEMR	−57.56	14.59	−0.11	**−57.36**	**16.04**	**0.00**
	DFM	−0.23	49.40	−28.75	**0.18**	**46.59**	**−33.56**
Trial 5, genetic	ELSA	0.00	0.00	0.00	**0.00**	**0.00**	**0.00**
	AEML	57.94	16.81	0.23	**58.13**	**15.51**	**-3.14**
	AEMR	−57.90	14.79	−0.06	**−57.35**	**16.07**	**0.00**
	DFM	0.13	49.75	−29.07	**0.19**	**46.51**	**−33.67**
Trial 1, F-solve	ELSA	0.00	0.00	0.00	0.00	0.00	0.00
	AEML	58.00	17.10	−0.19	58.16	15.75	0.34
	AEMR	−57.46	14.89	−0.20	−57.36	15.96	0.41
	DFM	−0.11	49.63	−28.69	0.96	50.26	−27.74
Trial 2, F-solve	ELSA	0.00	0.00	0.00	0.00	0.00	0.00
	AEML	58.07	16.73	0.24	58.20	15.59	0.49
	AEMR	−57.44	14.82	0.15	−57.32	16.11	0.46
	DFM	−0.18	49.57	−28.71	1.13	50.44	−27.41
Trial 3, F-solve	ELSA	0.00	0.00	0.00	0.00	0.00	0.00
	AEML	57.98	17.13	0.08	58.09	16.02	−0.13
	AEMR	−57.90	15.00	0.22	−57.43	15.70	0.55
	DFM	0.09	49.73	−28.79	0.59	49.99	−28.24
Trial 4, F-solve	ELSA	0.00	0.00	0.00	0.00	0.00	0.00
	AEML	57.78	16.98	−0.16	58.00	16.34	0.36
	AEMR	−57.56	14.59	−0.11	−57.52	15.37	0.38
	DFM	−0.23	49.40	−28.75	0.47	50.26	−27.75
Trial 5, F-solve	ELSA	0.00	0.00	0.00	0.00	0.00	0.00
	AEML	57.94	16.81	0.23	58.12	15.90	0.30
	AEMR	−57.90	14.79	−0.06	−57.40	15.82	0.18
	DFM	0.13	49.75	−29.07	0.89	50.03	−28.16

AEML, left auditory external meatus; AEMR, right auditory external meatus; DFM, dorsum foramen magnum.
The bold formatting indicates that in these trials, the points were almost identical.

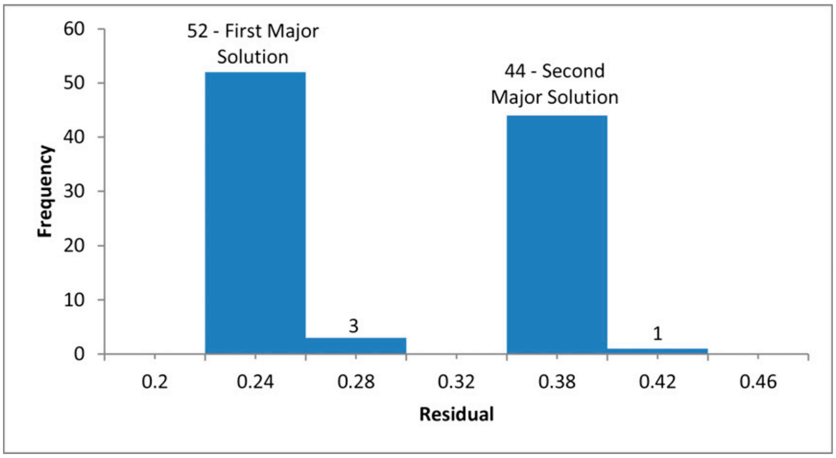

Figure 2 Histogram of 100 sample convergence results for 6-point algorithm

4-point algorithm increased the distance error seen between AEML, AEMR, DFM and menton right. It is suggested that this occurs because there is the potential for an uneven landmark locating error for the control points. This may cause the correction factors to overcompensate the correction of one point while improving the others, and thus increase the error seen for that specific point. Despite this, both algorithms significantly decrease the average distance error observed between AEML, AEMR, DFM and the control points on average.

As can be seen in Table 4, the average error seen in these distances between the first image and the second uncorrected image is 1.64 mm. This average error drops to 1.48 mm when corrected with the 4-point algorithm and further drops to 1.24 mm when corrected with the 6-point algorithm. These results demonstrate that the 6-point algorithm is capable of increasing intrapoint reliability between images by a greater degree than the previously introduced 4-point algorithm.

Table 3 Clinical results of ten real patients

Average error between AEML/AEMR/DFM		*Standard deviation (mm)*
(a) Infraorbitale left distance errors (mm)		
Uncorrected	1.93	0.62
Corrected using 4-point method	1.41	0.10
Corrected using 6-point method	1.09	0.24
(b) Infraorbitale right distance errors (mm)		
Uncorrected	1.66	0.66
Corrected using 4-point method	1.26	0.15
Corrected using 6-point method	0.95	0.15
(c) Menton left distance errors (mm)		
Uncorrected	1.65	0.46
Corrected using 4-point method	1.63	0.21
Corrected using 6-point method	1.58	0.43
(d) Menton right distance errors		
Uncorrected	1.34	0.89
Corrected using 4-point method	1.62	0.58
Corrected using 6-point method	1.32	0.38

AEML, left auditory external meatus; AEMR, right auditory external meatus; DFM, dorsum foramen magnum.

Discussion

The cranial base is the most stable region in the craniofacial part of the body because it is believed to achieve maximal growth early and before adolescence.[24] The anatomical structures of the cranial base have thus been widely used as the reference points in the superimposition of 2D cephalograms for diagnosis, assessment of change owing to growth of relevant structures and evaluation of treatment efficacy. Although, historically, scientists have been unable to prove that there is no significant change in the cranial base, it is now possible to assess its stability in the light of technological advances. Since its introduction, the role of CBCT has expanded from that of an auxiliary diagnostic tool to include numerous applications, such as assessment of 3D landmark location, shape and size of hard- and soft-tissue without the image distortion, magnification and incorrect landmark positioning associated with 2D cephalograms.[16,25–27] Even with all those benefits, caution is still needed when acquiring these types of images. Radiation exposures are lower than traditional medical CT but higher than traditional cephalometric X-rays. An example of this is mentioned by Carlson et al[28] where the effective dose from a typical orthodontic CBCT scan—large field of view scan using a Next-Generation i-CAT machine—is 74 μSv, whereas digital lateral cephalometric radiography exposes patients to approximately 5.6 μSv of radiation. It should be noted that many have compared these doses with 1 week of urban environment exposure or flights.[29] Our retrospective study used existing images. The aim is to

Table 4 Clinical results of ten real patients, overall average distance errors

Overall average distance errors (mm)		*Standard deviation (mm)*
Uncorrected	1.64	0.62
Corrected using 4-point method	1.48	0.32
Corrected using 6-point method	1.24	0.37

improve the current methods of determining treatment-based skeletal changes using technology widely used by clinicians. By our proposed method, and by using past data, we can minimize the current use of CBCT scans, which we believe should be minimized during treatment. CBCT has become more widely available to the dental field, and its increasing role in diagnosis and treatment necessitates the need for a standardized reference system with stable anatomical structures as the reference points. Greater use is seen for superimpositioning of 3D images, but this led to new challenges. A few methods have been developed and are being tested to accomplish accurate superimposition. One method is using greyscales to superimpose images as Cevidanes et al[5,30] used to determine the treatment changes associated with orthognathic surgery. The basis of the method is to mask all skeletal structures so that only the cranial base is used for superimposition. It compares the grey-level intensity of each voxel in the cranial base to obtain a best fit of both images. The final output obtained by this method is shown in colour-coded differences between surfaces. Results obtained are only reported as changes in two dimensions, for example, displacement outside or inside of the mandibular rami and condyles.

Another approach towards superimposing 3D images uses optimization analysis. This analysis involves minimizing the total root mean square error found over a series of fixed landmark positions, also known as best-fit analysis. Landmarks have been used since the beginning of cephalometric radiography, and dentists have been trained to identify landmarks and use these to diagnose and treat patients. Recently, Lagravère et al[21] proposed using a 4-point optimization procedure to correct for user errors. The optimization procedure involved the location of three points, the left and right AEM and the DFM, on an image of a patient relative to their location on a previous image. This problem, named here the 4-point algorithm, had nine constraint equations, nine variables and used a Newton–Rhapson algorithm to obtain an exact solution to the problem. The constraint equations related the distances and angles between points in each image. The variables were nine measurement error correction factors, one for each axis (x, y and z) of each movable point (AEML, AEMR and DFM). The non-linear solver, in this case a Newton–Rhapson algorithm, is used to find the values of the measurement error correction factors needed to make all constraint equations equal in each image. After extensive use of the algorithm, it was found that there were multiple exact solutions. It was thus concluded that a more accurate method for obtaining the corrections was necessary to obtain a unique solution. The new optimization formulation, described in the Materials and methods section, named here the 6-point algorithm, not only optimizes the location of the same three points (*i.e.* AEML, AEMR and DFM) but also includes two additional points in each image. The two new points are used to help obtain a specific solution each time. The two new points are both foramen ovale (right and left) that have been reported to have a high intrareliability, similar to that found for the foramen spinosum.[8]

It has been reported that intrareliability of the landmarks forming the co-ordinate system (ELSA, AEML, AEMR and DFM) was excellent in all axes.[17] The addition of two extra landmarks (FOR and FOL) in the optimization analysis was shown to reduce the envelope of error when determining the co-ordinate system. Future research is needed to verify alternative options towards this superimposition technique. The addition of two extra points to the original four points improved the optimization. A next step would be to try new points close to the vicinity of the original ones and to use greyscales on the area surrounding the six points used in the present method. Other methods such as merging two volumes[30] and minimizing the least-square error of a function (usually colour scale) between two images[31] should also be studied. The method proposed by Dranischnikow et al[31] has proven to be quite capable of matching complex geometries. The method proposed by Dranischnikow et al was successfully used to align the sectional cone beam CT images of a jaw and MR or CT images of lungs. The proposed method by Dranischnikow et al is likely to be more accurate and it does not depend on the landmark identification, thereby removing any operator errors; therefore, it will be investigated in the future. However, it is a more complex method to implement compared with the proposed approach. Using our simplified approach, our findings are already within the clinical error range required for orthodontic treatment, thereby providing a trade-off between the ease of implementation and the desired result accuracy.

In conclusion, a novel method of optimizing the overlay of 3D images using a 6-point correction algorithm was introduced and examined. This method demonstrated greater reliability and reproducibility than the previous 4-point correction algorithm and showed greater resiliency to landmark identification error. When analysing real patient data, it was found that the 6-point algorithm reduced errors between images and increased intrapoint reliability compared with both uncorrected images and images corrected with the 4-point algorithm.

References

1. Nada RM, Maal TJ, Breuning KH, Bergé SJ, Mostafa YA, Kuijpers-Jagtman AM. Accuracy and reproducibility of voxel based superimposition of cone beam computed tomography models on the anterior cranial base and the zygomatic arches. *PLoS One* 2011; **6**: e16520. doi: 10.1371/journal.pone.0016520.
2. Mah JK, Huang JC, Choo H. Practical applications of cone-beam computed tomography in orthodontics. *J Am Dent Assoc* 2010; **141**: 7S–13S.
3. Grauer D, Cevidanes LS, Proffit WR. Working with DICOM craniofacial images. *Am J Orthod Dentofacial Orthop* 2009; **136**: 460–470. doi: 10.1016/j.ajodo.2009.04.016.

4. Berkowitz S. A multicenter retrospective 3D study of serial complete unilateral cleft lip and palate and complete bilateral cleft lip and palate casts to evaluate treatment: part 1–the participating institutions and research aims. *Cleft Palate Craniofac J* 1999; **36**: 413–424.
5. Cevidanes LH, Bailey LJ, Tucker GR Jr, Styner MA, Mol A, Phillips CL, et al. Superimposition of 3D cone-beam CT models of orthognathic surgery patients. *Dentomaxillofac Radiol* 2005; **34**: 369–375. doi: 10.1259/dmfr/17102411.
6. Cevidanes LH, Bailey LJ, Tucker SF, Styner MA, Mol A, Phillips CL, et al. Three-dimensional cone-beam computed tomography for assessment of mandibular changes after orthognathic surgery. *Am J Orthod Dentofacial Orthop* 2007; **131**: 44–50. doi: 10.1016/j.ajodo.2005.03.029.
7. Lagravère MO, Hansen L, Harzer W, Major PW. Plane orientation for standardization in 3-dimensional cephalometric analysis with computerized tomography imaging. *Am J Orthod Dentofacial Orthop* 2006; **129**: 601–604. doi: 10.1016/j.ajodo.2005.11.031.
8. Lagravère MO, Gordon JM, Flores-Mir C, Carey J, Heo G, Major PW. Cranial base foramen location accuracy and reliability in cone-beam computerized tomography. *Am J Orthod Dentofacial Orthop* 2011; **139**: e203–e210. doi: 10.1016/j.ajodo.2009.06.027.
9. Bjork A. The use of metallic implants in the study of facial growth in children: method and application. *Am J Phys Anthropol* 1968; **29**: 243–254.
10. Melsen B, Melsen F. The postnatal development of the palatomaxillary region studied on human autopsy material. *Am J Orthod* 1982; **82**: 329–342.
11. Waitzman AA, Posnick JC, Armstrong DC, Pron GE. Craniofacial skeletal measurements based on computed tomography: Part II. Normal values and growth trends. *Cleft Palate Craniofac J* 1992; **29**: 118–128. doi: 10.1597/1545-1569(1992)029<0118:CSMBOC>2.3.CO;2.
12. Sgouros S, Natarajan K, Hockley AD, Goldin JH, Wake M. Skull base growth in childhood. *Pediatr Neurosurg* 1999; **31**: 259–268. doi: 10.1159/000028873.
13. Gribel BF, Gribel MN, Frazäo DC, McNamara JA Jr, Manzi FR. Accuracy and reliability of craniometric measurements on lateral cephalometry and 3D measurements on CBCT scans. *Angle Orthod* 2011; **81**: 26–35. doi: 10.2319/032210-166.1.
14. Tausche E, Hansen L, Hietschold V, Lagravère MO, Harzer W. Three-dimensional evaluation of surgically assisted implant bone-borne rapid maxillary expansion: a pilot study. *Am J Orthod Dentofacial Orthop* 2007; **131**: S92–S99.
15. Lagravère MO, Gordon JM, Guedes IH, Flores-Mir C, Carey JP, Heo G, et al. Reliability of traditional cephalometric landmarks as seen in three-dimensional analysis in maxillary expansion treatments. *Angle Orthod* 2009; **79**: 1047–1056.
16. Lagravère MO, Low C, Flores-Mir C, Chung R, Carey JP, Heo G, et al. Intraexaminer and interexaminer reliabilities of landmark identification on digitized lateral cephalograms and formatted 3-dimensional cone-beam computerized tomography images. *Am J Orthod Dentofacial Orthop* 2010; **137**: 598–604.
17. Lagravère MO, Major PW, Carey J. Sensitivity analysis for plane orientation in three-dimensional cephalometric analysis based on superimposition of serial cone beam computed tomography images. *Dentomaxillofac Radiol* 2010; **39**: 400–408.
18. Seckel NG, van der Tweel I, Elema GA, Specken TF. Landmark positioning on maxilla of cleft lip and palate infant–a reality? *Cleft Palate Craniofac J* 1995; **32**: 434–441. doi: 10.1597/1545-1569(1995)032<0434:LPOMOC>2.3.CO;2.
19. Sachdeva RC. SureSmile technology in a patient–centered orthodontic practice. *J Clin Orthod* 2001; **35**: 245–253.
20. Ashmore JL, Kurland BF, King GJ, Wheeler TT, Ghafari J, Ramsay DS. A 3-dimensional analysis of molar movement during headgear treatment. *Am J Orthod Dentofacial Orthop* 2002; **121**: 18–29; discussion 29–30.
21. Lagravère MO, Secanell M, Major PW, Carey J. Optimization analysis for plane orientation in three-dimensional cephalometric analysis of serial cone-beam computerized tomography images. *Oral Surg Oral Med Oral Pathol Oral Radiol Endod* 2011; **111**: 771–777. doi: 10.1016/j.tripleo.2011.02.017.
22. Lagravère MO, Major PW. Proposed reference point for 3-dimensional cephalometric analysis with cone-beam computerized tomography. *Am J Orthod Dentofacial Orthop* 2005; **128**: 657–660. doi: 10.1016/j.ajodo.2005.07.003.
23. Kim IY, de Weck OL. Advanced weighted sum method for multiobjective optimization: a new methods for Pareto front generation. *Struct Multidisc Optim* 2006; **31**: 105–116.
24. Friede H. Normal development and growth of the human neurocranium and cranial base. *Scand J Plast Reconstr Surg* 1981; **15**: 163–169.
25. Major PW, Johnson DE, Hesse KL, Glover KE. Landmark identification error in posterior anterior cephalometrics. *Angle Orthod* 1994; **64**: 447–454. doi: 10.1043/0003-3219(1994)064<0447:LIEIPA>2.0.CO;2.
26. Athanasiou AE. *Orthodontic cephalometry.* London and Baltimore: Mosby-Wolfe; 1995.
27. Halazonetis DJ. From 2-dimensional cephalograms to 3-dimensional computed tomography scans. *Am J Orthod Dentofacial Orthop* 2005; **127**: 627–637. doi: 10.1016/j.ajodo.2005.01.004.
28. Carlson S, Graham J, Harrell WE Jr, Lin EY, Molen A, Womack R. The truth about CBCT radiation. *Orthotown* 2011; 62–68.
29. Bartlett DT, Hager LG, Irvine D, Bagshaw M. Measurements on Concorde of the Cosmic Radiation Field at Aviation Altitudes. *Radiat Prot Dosimetry* 2000; **91**: 365–376.
30. Cevidanes LH, Styner MA, Proffit WR. Image analysis and superimposition of 3-dimensional cone-beam computed tomography models. *Am J Orthod Dentofacial Orthop* 2006; **129**: 611–618. doi: 10.1016/j.ajodo.2005.12.008.
31. Dranischnikow E, Schömer E, Schwanecke U, Schulze R, Brüllmann D. A parallel approach for alignment of multi-modal gridbased data. *Proceedings of IADIS AC*; 2009; **1**: 330–337.
32. Garret N. *Vanderplaats, numerical optimization techniques for engineering design: with applications.* New York, NY: McGraw-Hill College; 1984.

Appendix

This appendix provides a complete list of objective functions associated with the multiobjective optimization problem in Equation (1). Objective functions involving points AEML, AEMR and DFM are indicated as f_i and are known as the primary objectives, since they involve the points that define the co-ordinate system and are also the points for which the corrections are obtained. Objectives involving RFO and LFO are indicated as g_i and are known as the secondary objectives. They are used to increase the accuracy of the correction calculations. Note that points RFO and LFO will not be used to define the co-ordinate system.

The objective functions below, f_1–f_5 and g_1–g_6, are aimed at quantifying the difference between Image 1 and Image 2 of the relative distance between points and they are given by

$$\left.\begin{aligned}
\frac{\|\mathbf{x}^1_{\mathrm{AEML}}\|-\|\mathbf{x}^2_{\mathrm{AEML}}\|}{n_\mathrm{d}}&=f_1\\
\frac{\|\mathbf{x}^1_{\mathrm{AEMR}}\|-\|\mathbf{x}^2_{\mathrm{AEMR}}\|}{n_\mathrm{d}}&=f_2\\
\frac{\|\mathbf{x}^1_{\mathrm{DFM}}\|-\|\mathbf{x}^2_{\mathrm{DFM}}\|}{n_\mathrm{d}}&=f_3\\
\frac{\|\mathbf{x}^1_{\mathrm{AEML}}-\mathbf{x}^1_{\mathrm{AEMR}}\|-\|\mathbf{x}^2_{\mathrm{AEML}}-\mathbf{x}^2_{\mathrm{AEMR}}\|}{n_\mathrm{d}}&=f_4\\
\frac{\|\mathbf{x}^1_{\mathrm{AEML}}-\mathbf{x}^1_{\mathrm{DFM}}\|-\|\mathbf{x}^2_{\mathrm{AEML}}-\mathbf{x}^2_{\mathrm{DFM}}\|}{n_\mathrm{d}}&=f_5\\
\frac{\|\mathbf{x}^1_{\mathrm{AEMR}}-\mathbf{x}^1_{\mathrm{DFM}}\|-\|\mathbf{x}^2_{\mathrm{AEMR}}-\mathbf{x}^2_{\mathrm{DFM}}\|}{n_\mathrm{d}}&=f_6\\
\frac{\|\mathbf{x}^1_{\mathrm{AEML}}-\mathbf{x}^1_{\mathrm{RFO}}\|-\|\mathbf{x}^2_{\mathrm{AEML}}-\mathbf{x}^2_{\mathrm{RFO}}\|}{n_\mathrm{d}}&=g_1\\
\frac{\|\mathbf{x}^1_{\mathrm{AEML}}-\mathbf{x}^1_{\mathrm{LFO}}\|-\|\mathbf{x}^2_{\mathrm{AEML}}-\mathbf{x}^2_{\mathrm{LFO}}\|}{n_\mathrm{d}}&=g_2\\
\frac{\|\mathbf{x}^1_{\mathrm{AEMR}}-\mathbf{x}^1_{\mathrm{RFO}}\|-\|\mathbf{x}^2_{\mathrm{AEMR}}-\mathbf{x}^2_{\mathrm{RFO}}\|}{n_\mathrm{d}}&=g_3\\
\frac{\|\mathbf{x}^1_{\mathrm{AEMR}}-\mathbf{x}^1_{\mathrm{LFO}}\|-\|\mathbf{x}^2_{\mathrm{AEMR}}-\mathbf{x}^2_{\mathrm{LFO}}\|}{n_\mathrm{d}}&=g_4\\
\frac{\|\mathbf{x}^1_{\mathrm{DFM}}-\mathbf{x}^1_{\mathrm{RFO}}\|-\|\mathbf{x}^2_{\mathrm{DFM}}-\mathbf{x}^2_{\mathrm{RFO}}\|}{n_\mathrm{d}}&=g_5\\
\frac{\|\mathbf{x}^1_{\mathrm{DFM}}-\mathbf{x}^1_{\mathrm{LFO}}\|-\|\mathbf{x}^2_{\mathrm{DFM}}-\mathbf{x}^2_{\mathrm{LFO}}\|}{n_\mathrm{d}}&=g_6
\end{aligned}\right\}\tag{A1}$$

where $n_\mathrm{d}=\frac{1}{6}\sum_{i=1}^{6}f_{i,\mathrm{initial}}+\frac{1}{6}\sum_{j=1}^{6}g_{j,\mathrm{initial}}$ is a constant value used to normalize the equations as discussed below.

The co-ordinate of a point is represented by $\mathbf{x}$. The superscript represents the image and the subscript represents the point. For example, symbol $\mathbf{x}^1_{\mathrm{AEML}}$ represents the co-ordinates of AEML in Image 1. $\mathbf{x}^2_{\mathrm{AEML}}$ are the co-ordinates of AEML in Image 2. Since the points representing the co-ordinate system are corrected during the optimization, the co-ordinates of AEML in Image 2 are given as

$$\mathbf{x}^2_{\mathrm{AEML}}\equiv\mathbf{x}^2_{\mathrm{AEML,original}}+\delta\mathbf{u}_{\mathrm{AEML}}\tag{A2}$$

and $\delta\mathbf{u}_{\mathrm{AEML}}$ is the unknown error correction vector. Note that for RFO, $\mathbf{x}^2_{\mathrm{RFO}}\equiv\mathbf{x}^2_{\mathrm{RFO,original}}$, *i.e.* the co-ordinates for RFO and LFO do not change during the optimization since only the points that form the co-ordinate system are corrected.

The distance between points is computed using the Euclidean distance. Symbol $\|\|$ in the equations above therefore represents the Euclidean distance between two points. When only one point is shown, it represents the distance between that point and ELSA. For example, equation f_1 computes the difference between the relative distance from ELSA to AEML in Image 1 and Image 2, once the correction $\delta\mathbf{u}_{\mathrm{AEML}}$, $\delta\mathbf{u}_{\mathrm{AEMR}}$ and $\delta\mathbf{u}_{\mathrm{DFM}}$ has been applied. Note that equations f_1–f_3 can only be applied to AEML, AEMR and DFM, since these are the only points that are moved during the optimization problem. The distance between ELSA and LFO and RFO is the same during the optimization process.

In addition to reducing the relative distance between points, the difference between images of the relative angles between points should also be minimized. Therefore, objectives f_7–f_9 and g_7–g_{12} below aim at quantifying the difference between Image 1 and Image 2 of the relative angle between points. To achieve this goal, the objective functions return the difference between the cosine of the relative angle between points, thereby providing a normalized value between zero and one. The equations are given as

$$\left.\begin{aligned}
\frac{(\mathbf{x}^1_{\mathrm{AEML}}\cdot\mathbf{x}^1_{\mathrm{AEMR}})}{\|\mathbf{x}^1_{\mathrm{AEML}}\|\|\mathbf{x}^1_{\mathrm{AEMR}}\|}-\frac{(\mathbf{x}^2_{\mathrm{AEML}}\cdot\mathbf{x}^2_{\mathrm{AEMR}})}{\|\mathbf{x}^2_{\mathrm{AEML}}\|\|\mathbf{x}^2_{\mathrm{AEMR}}\|}&=f_7\\
\frac{(\mathbf{x}^1_{\mathrm{AEML}}\cdot\mathbf{x}^1_{\mathrm{DFM}})}{\|\mathbf{x}^1_{\mathrm{AEML}}\|\|\mathbf{x}^1_{\mathrm{DFM}}\|}-\frac{(\mathbf{x}^2_{\mathrm{AEML}}\cdot\mathbf{x}^2_{\mathrm{DFM}})}{\|\mathbf{x}^2_{\mathrm{AEML}}\|\|\mathbf{x}^2_{\mathrm{DFM}}\|}&=f_8\\
\frac{(\mathbf{x}^1_{\mathrm{AEMR}}\cdot\mathbf{x}^1_{\mathrm{DFM}})}{\|\mathbf{x}^1_{\mathrm{AEMR}}\|\|\mathbf{x}^1_{\mathrm{DFM}}\|}-\frac{(\mathbf{x}^2_{\mathrm{AEMR}}\cdot\mathbf{x}^2_{\mathrm{DFM}})}{\|\mathbf{x}^2_{\mathrm{AEMR}}\|\|\mathbf{x}^2_{\mathrm{DFM}}\|}&=f_9\\
\frac{(\mathbf{x}^1_{\mathrm{AEML}}\cdot\mathbf{x}^1_{\mathrm{RFO}})}{\|\mathbf{x}^1_{\mathrm{AEML}}\|\|\mathbf{x}^1_{\mathrm{RFO}}\|}-\frac{(\mathbf{x}^2_{\mathrm{AEML}}\cdot\mathbf{x}^2_{\mathrm{RFO}})}{\|\mathbf{x}^2_{\mathrm{AEML}}\|\|\mathbf{x}^2_{\mathrm{RFO}}\|}&=g_7\\
\frac{(\mathbf{x}^1_{\mathrm{AEML}}\cdot\mathbf{x}^1_{\mathrm{LFO}})}{\|\mathbf{x}^1_{\mathrm{AEML}}\|\|\mathbf{x}^1_{\mathrm{LFO}}\|}-\frac{(\mathbf{x}^2_{\mathrm{AEML}}\cdot\mathbf{x}^2_{\mathrm{LFO}})}{\|\mathbf{x}^2_{\mathrm{AEML}}\|\|\mathbf{x}^2_{\mathrm{LFO}}\|}&=g_8\\
\frac{(\mathbf{x}^1_{\mathrm{AEMR}}\cdot\mathbf{x}^1_{\mathrm{RFO}})}{\|\mathbf{x}^1_{\mathrm{AEMR}}\|\|\mathbf{x}^1_{\mathrm{RFO}}\|}-\frac{(\mathbf{x}^2_{\mathrm{AEMR}}\cdot\mathbf{x}^2_{\mathrm{RFO}})}{\|\mathbf{x}^2_{\mathrm{AEMR}}\|\|\mathbf{x}^2_{\mathrm{RFO}}\|}&=g_9\\
\frac{(\mathbf{x}^1_{\mathrm{AEMR}}\cdot\mathbf{x}^1_{\mathrm{LFO}})}{\|\mathbf{x}^1_{\mathrm{AEMR}}\|\|\mathbf{x}^1_{\mathrm{LFO}}\|}-\frac{(\mathbf{x}^2_{\mathrm{AEMR}}\cdot\mathbf{x}^2_{\mathrm{LFO}})}{\|\mathbf{x}^2_{\mathrm{AEMR}}\|\|\mathbf{x}^2_{\mathrm{LFO}}\|}&=g_{10}\\
\frac{(\mathbf{x}^1_{\mathrm{DFM}}\cdot\mathbf{x}^1_{\mathrm{RFO}})}{\|\mathbf{x}^1_{\mathrm{DFM}}\|\|\mathbf{x}^1_{\mathrm{RFO}}\|}-\frac{(\mathbf{x}^2_{\mathrm{DFM}}\cdot\mathbf{x}^2_{\mathrm{RFO}})}{\|\mathbf{x}^2_{\mathrm{DFM}}\|\|\mathbf{x}^2_{\mathrm{RFO}}\|}&=g_{11}\\
\frac{(\mathbf{x}^1_{\mathrm{DFM}}\cdot\mathbf{x}^1_{\mathrm{LFO}})}{\|\mathbf{x}^1_{\mathrm{DFM}}\|\|\mathbf{x}^1_{\mathrm{LFO}}\|}-\frac{(\mathbf{x}^2_{\mathrm{DFM}}\cdot\mathbf{x}^2_{\mathrm{LFO}})}{\|\mathbf{x}^2_{\mathrm{DFM}}\|\|\mathbf{x}^2_{\mathrm{LFO}}\|}&=g_{12}
\end{aligned}\right\}\tag{A3}$$

where $\cdot$ represents the dot product between the two points and $\|\|$ again represents the Euclidean distance between two points. For example, $\mathbf{x}^1_{\mathrm{AEML}}\cdot\mathbf{x}^1_{\mathrm{AEMR}}$ represents the dot product between ELSA and AEML and between ELSA and AEMR as shown in Figure A1.

In multiobjective optimization problems, it is important that all objectives are of similar sizes, otherwise the optimization algorithm will not converge or it will converge to solutions that are not optimal. To correct this, normalization of all objectives was performed so that each of the objectives would be bound between zero

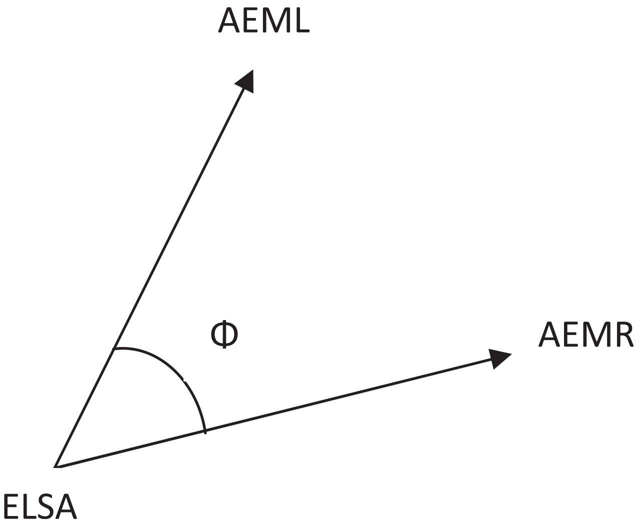

Figure A1 Angle between AEML and AEMR. AEML, left auditory external meatus; AEMR, right auditory external meatus.

and one, preventing any single residual from being significantly larger than the rest and having an overwhelming influence on the solution.[32] After various methods of normalization were explored, it was decided that, for distances, each distance constraint equation would be divided by the average sum of all the initial residuals of these distance constraint equations. Each term of each angle constraint equation was already between zero and one.